Copper ion/gallic acid MOFs-laden adhesive pomelo peel sponge effectively treats biofilm-infected skin wounds and improves healing quality

Jianqiu Yang [a,b,1], Zhenzhen Huang [b,1], Jiang Tan [b,c,d], Jingye Pan [c,d,**], Shixuan Chen [b,c,*], Wenbing Wan [a,***]

[a] Department of Orthopaedic Surgery, The Second Affiliated Hospital of Nanchang University, Nanchang, Jiangxi 330006, China
[b] Zhejiang Engineering Research Center for Tissue Repair Materials, Wenzhou Institute, University of Chinese Academy of Sciences, Wenzhou, Zhejiang 325000, China
[c] Key Laboratory of Intelligent Treatment and Life Support for Critical Diseases of Zhejiang Province, The First Affiliated Hospital of Wenzhou Medical University, Wenzhou, Zhejiang 325000, China
[d] Zhejiang Engineering Research Center for Hospital Emergency and Process Digitization, The First Affiliated Hospital of Wenzhou Medical University, Wenzhou, Zhejiang 325000, China

ARTICLE INFO

ABSTRACT

Bacterial infection and scar formation remain primary challenges in wound healing. To address these issues, we developed a decellularized pomelo peel (DPP) functionalized with an adhesive PVA-TSPBA hydrogel and antibacterial gallic acid/copper MOFs. The hybrid wound dressing demonstrates favorable biocompatibility. It does not impede the proliferation of fibroblasts or immune cells and can stimulate fibroblast migration, endothelial angiogenesis, and M2 macrophage polarization. Additionally, the dressing can scavenge reactive oxygen species (ROS) and provide antioxidant effects. Furthermore, DPP + MOF@Gel effectively inhibits the viability of *S. aureus* and *E. coli* in vitro and in vivo. The histological observations revealed enhanced granulation tissue formation, re-epithelialization, and angiogenesis in the DPP + MOF@Gel group compared to other groups. The local immune response also shifted from a pro-inflammatory to a pro-regenerative status with DPP + MOF@Gel treatment. The skin incision stitching experiment further exhibits DPP + MOF@Gel could reduce scar formation during wound healing. Taken together, the hybrid DPP + MOF@Gel holds great promise for treating bacteria-infected skin wounds and inhibiting scar formation during wound healing.

1. Introduction

Nature offers abundant raw materials for wound healing. In ancient China, people lacked access to modern wound dressings and used natural medicinal herbs instead. They would mash the herbs and apply them to wounds to promote healing. One renowned example is Shiunko, which effectively treats chapped skin, frostbite, trauma, and burns by stimulating granulation tissue and re-epithelialization [1,2]. Besides Shiunko, there are other potential medicinal plants. Pomelo peel is a by-product of pomelo consumption and is rich in nutrients and bioactive compounds. It contains compounds such as pectin, polysaccharides, phenolic acids, flavonoids, coumarins, carotenoids, and aroma-active volatiles [3]. Among them, coumarin compounds exhibited the same anti-inflammatory effect as dexamethasone, which could effectively inhibit edema in vivo and the production of pro-inflammatory cytokines such as IL-1β, TNF-α, and prostaglandin 2 in vitro [4]. In addition, the residual component, phenolic acids, and flavonoids show considerable antioxidant properties. It revealed significant dose-dependent inhibition of DPPH activity, with an IC50 of 68.55 μg/mL compared to 55.87 μg/mL for vitamin C as the standard control [5]. Modulating

---

Schematic 1. (A) The schematic diagram illustrates the preparation of the decellularized pomelo peel coated with gallic acid/copper MOFs loaded PVA-TSPBA hydrogel was developed for bacteria-infected wound healing (B) and improved healing quality (C).

inflammation and oxidative stress are pivotal targets for optimizing the wound microenvironment to establish a favorable wound bed for healing. Moreover, such anti-inflammatory and anti-oxidative strategies can reduce scar formation and improve healing quality [6,7]. Reducing scar formation represents a pressing need in the current landscape of wound management. Thus, the pomelo peel has the potential to become a wound dressing, which can promote wound healing and improve the quality of healing.

In previous work, we decellularized pomelo peel (DPP) and fabricated it into a natural cellulose wound dressing. However, our pre-research studies find it still has some inherent challenges for wound management. Firstly, it is prone to dehydration and becomes rigid upon moisture loss. Secondly, pomelo peel is difficult to adhere onto wounds and liable to detach after application. Finally, some wounds present with infection complications. Herein, we try to modify pomelo peel and endow it with more functions to make it more suitable for the application of wound repair. Adhesive hydrogel can be used as a coating material for DPP to address the aforementioned issues. It is able to not only enhance the adhesion of the DPP, but also prevent moisture loss. Moreover, incorporating anti-bacterial agents into the coated hydrogel could achieve the anti-bacterial properties of the DPP. In recent years, the biocompatible PVA-TSPBA hydrogel has attracted more attention. It has been widely used to deliver bioactive factors [8–10], stem cells [11]. Additionally, the PVA-TSPBA hydrogel is a reactive oxygen species (ROS)-sensitive hydrogel capable of scavenging ROS produced in the tissue microenvironment [12,13]. Therefore, the PVA-TSPBA hydrogel is selected as a coating material to modify the DPP.

After addressing the adhesion issues of the DPP, we subsequently consider incorporating antibacterial agents into the coated hydrogel to impart antibacterial properties to the DPP. Metal ions play an important role in the anti-bacterial field, which can avoid drug resistance. For example, nanosilver particles or silver ions have been widely used in various wound treatments [14,15]. However, more and more evidence shows that silver ions have apparent cytotoxicity and organ accumulation problems, and silver can hinder the process of re-epithelialization in the later stage of wound repair [16]. By comparison, copper clusters are potential alternatives. It has been used to inhibit bacteria infection in agriculture for decades [17]. And the biosafety of copper ions is better than silver. Because copper is a necessary element of the human body and can be metabolized by the human body [18]. In addition, copper clusters are readily available and inexpensive [19]. Numerous strategies exist for delivering copper ions, with metal-organic frameworks (MOFs) representing one potential approach due to their excellent properties, such as structural diversity, porosity, tailorability, and high specific surface area. Gallic acid, a bioligand, is a naturally occurring polyphenolic active molecule that can exert anti-inflammatory effects by reducing the expression of pro-inflammatory cytokines such as interleukin-1β (IL-1β) and tumor necrosis factor-α (TNF-α) [20,21]. It can form MOF particles with copper ions through self-assembly.

Taken together, we utilized DPP as the substrate material, PVA-TSPBA hydrogel as the coating to improve DPP's adhesive and moisture retention properties, and gallic acid/Cu MOFs as an antimicrobial agent (Schematic 1). We hypothesize that the DPP coated with gallic acid/copper MOFs loaded PVA-TSPBA hydrogel (DPP + MOF@Gel) could address the bacteria infection wound healing and improve healing quality. In vitro, we examined the adhesive properties, biocompatibility, antimicrobial effects, anti-inflammatory activity, and antioxidant capacity of DPP + MOF@Gel. In vivo, we evaluated the impact of DPP + MOF@Gel on granulation tissue formation, angiogenesis, re-epithelialization, and scar formation during wound healing.

2. Materials and methods

2.1. Reagents

All the pomelos used in the experiment were purchased from Yonghui supermarket (Shatian pomelo, China). Dulbecco's modified Eagle culture medium (DMEM, catalog number: 11965118), penicillin-streptomycin (PS, catalog number: 15140122), and fetal bovine serum (FBS, catalog number:10099-141C) were purchased from Invitrogen (California, USA). Sodium hypochlorite (catalog number: S101636) and Triton-X100 (catalog number: T109027) are provided by Aladdin Biotechnology Co., Ltd., and Tris-HCl (pH = 8.5, catalog number: R23195) is purchased from Yuanye Biotechnology Co., Ltd. (Shanghai, China). Glutaraldehyde was purchased from Aladdin Biochemical Technology Co., Ltd. (catalog number: G105905, Shanghai, China). Ethanol was purchased from McLean Biochemical Technology Co., LTD (catalog number: E809063, Shanghai, China). The cell counting kit-8 (CCK-8) was purchased from Beyotime Biotech (catalog number: C0040, Shanghai, China), and the acridine orange/ethidium bromide staining kit was purchased from Merida Technology (catalog number: Shenzhen M247364, China). Anhydrous copper chloride (catalog number: C106775, Shanghai, China), Gallic acid (catalog number: G131992, Shanghai, China), 4-(bromomethyl) phenylboronic acid (catalog number: B181368, Shanghai, China), N, N, N′, N′- tetramethyl-1-mer 3-propane-diamine (catalog number: T106825, Shanghai, China) and tetrahydrofuran (catalog number: T120775, Shanghai, China) were purchased from Aladdin. Anti-CD31 rabbit polyclonal antibodies

(catalog number: GB-11063-2) were purchased from Abcam Group. Rabbit polyclonal Anti-CD206 rabbit pAb (catalog number: ab64693) and Mouse monoclonal Anti-iNOS antibody (catalog number: ab178945) were purchased from Abcam Group. 1,1-Diphenyl-2-trinitrophenylhydrazine (DPPH, Sigma-Aldrich, catalog number: 1898-66-4) was used to determine the free radical scavenging activity. Goat Anti-Rabbit IgG H&L (Alexa Fluor® 594, catalog number: ab150080) and Goat anti-mouse IgG H&L (Alexa Fluor® 488, catalog number: ab150113) were purchased from Abcam Group.

2.2. Preparation of copper ion/gallic acid MOFs

Firstly, 12.8 g of anhydrous copper chloride was dissolved in 500 mL of deionized water in a round-bottomed flask. Next, 10 g of gallic acid was added and stirred until fully dissolved. The pH of the solution was then adjusted to 7.5 using an 8 mol/L KOH solution. The mixture was heated in a muffle furnace at 140 °C for 24 h. Finally, the resulting light gray solid was isolated by centrifugation at 12,000 rpm and 4 °C for 15 min. The solid was washed three times with ultrapure water and dried at 37 °C to obtain the Cu/GA MOFs powder.

2.3. Characterization of Cu/GA MOFs

Cu/GA MOFs was characterized by Fourier-transform infrared spectroscopy (FTIR, Thermo Scientific Nicolet iS5), X-ray photoelectron spectroscopy (XPS, Thermo Scientific K-Alpha), and X-ray diffraction (XRD, Thermo Scientific K-Alpha). The internal structure of Cu/GA MOFs was visualized using scanning electron microscopy (SEM, TESCAN MIRA LMS) and transmission electron microscopy (TEM, FEI Talos F200S). Particle size distribution was analyzed by dynamic light scattering (DLS) using a nanoparticle size analyzer (Malvern Zetasizer Nano ZS90).

2.4. Preparation of decellularized pomelo peel sponge (DPP)

Pomelo peels were cut into 2 mm thick discs and soaked in a 10 % w/v SDS solution on a low-speed shaker at room temperature for 5 days. After 5 days, the samples were washed 3 times with ultrapure water and then soaked in 0.1 % Triton-X100 (v/v) and 10 % sodium hypochlorite (v/v) for 2 days. Next, the samples were incubated in Tris-HCl buffer (pH 8.5) for 2 days. Finally, the samples were sterilized by soaking in alcohol for 2 h, washed 3 times with sterile PBS, and lyophilized. The freeze-dried pieces were UV sterilized for 30 min and stored aseptically.

2.5. Synthesis of TSPBA linker

4-(Bromoethyl)phenylboronic acid (1 g, 4.6 mmol) and N,N,N′,N′-tetramethyl-1,3-propanediamine (0.2 g, 1.5 mmol) were added to N,N-dimethylformamide (DMF) (40 mL) and stirred at 60 °C for 24 h. Next, 100 mL of tetrahydrofuran (THF) was added to the supernatant to obtain a white solid precipitate, which was washed 3 times with THF. The white residue was resuspended in 20 mL of THF, centrifuged at 8000 rpm for 5 min at room temperature, and lyophilized to obtain 0.6 g of TSPBA as a white solid (70 % yield).

2.6. TSPBA NMR spectrum

The purified TSPBA powder was dissolved in deuterated DMSO and analyzed by 1H nuclear magnetic resonance (NMR) spectroscopy on a 400 MHz instrument (Bruker Avance III).

2.7. Swelling rate of PVA-TSPBA

The PVA-TSPBA hydrogels were lyophilized overnight and weighed to obtain the dry weight (Wb). The dried gels were immersed in PBS at 37 °C for 5, 15, 20, 25, 30, and 60 s, removed, and weighed wet to obtain Ww. The swelling ratio was calculated using the following equation: Swelling ratio = (Ww - Wb)/Wb.

2.8. Self-healing ability of coated hydrogels

The self-healing ability was evaluated by cutting two differently colored hydrogel strips in half and reconnecting them after exchanging the red and blue halves. Upon heating to 37 °C, permeation occurred between the disconnected hydrogel junctions.

2.9. Rheological experiment

The dynamic rheological behavior before and after gelation at 25 °C was assessed using a stress-controlled rheometer (Haake Mars 60) with a 25 mm aluminum parallel-plate geometry. The structural recovery was modeled by determining the modulus changes at 1 % and 300 % strain. Measurements were conducted under linear viscoelastic conditions with a 500 μm gap between plates.

2.10. Adhesion test and leakage test

For adhesion testing, 50 g cylindrical alloy samples were placed in air or water. An 8 mm diameter, 1 mm thick hydrogel disk was adhered to the alloy surface. Successful adhesion was indicated if the disk could lift the alloy using an 8 mm diameter iron rod. For leakage testing, a 5 mm hole was drilled in the bottom of a plastic water tank and covered with an 8 mm diameter, 1 mm thick hydrogel disk. The water was dyed blue for visualization. Leakage was evaluated by observing water flow before and after covering the hole with the hydrogel.

2.11. Preparation of hydrogel-coated decellularized pomelo peel sponge

The decellularized pomelo peel was soaked in 100 mL of a 10 % wt/wt PVA solution containing 250 μg/mL Cu/GA MOFs and vacuum infiltrated overnight. Next, 100 mL of a 3 wt% TSPBA solution was added to the surface of the decellularized pomelo peel to obtain the intelligent dressing modified with a ROS/pH dual-responsive adhesive coating.

2.12. Characterization of hydrogel-coated decellularized pomelo peel sponge

FTIR spectroscopy (Thermo Scientific Nicolet 6700) was used to analyze DPP, PVA, Cu/GA MOFs, DPP + Gel, and DPP + MOF@Gel to determine their chemical groups. The microstructure of the decellularized pomelo peel bright composite dressing was characterized by scanning electron microscopy (TESCAN Mira LMS). The drug release profile under various hydrogen peroxide concentrations (125 μM, 250 μM, 500 μM) and pH conditions (pH 7.4 PBS, pH 5.0 PBS) was measured by UV–vis spectrophotometry (Shanghai Meibao Instrument Co.). The mechanical properties of Gel (PVA-TSPBA), MOF@Gel, DPP + Gel, and DPP + MOF@Gel were evaluated by tensile, shear, and compression testing using an electromechanical universal tester (CMT6104, Mester Industrial). For tensile tests, samples were stretched at 2 mm/min until failure. For shear tests, samples were adhered between two pork skin slices and pulled apart at 2 mm/min. For compression tests, samples were compressed at 2 mm/min to 90 % strain. Water contact angles of DPP, DPP + Gel, and DPP + MOF@Gel were measured by goniometry (Lauda Scientific LSA100). Zeta potentials of MOF, DPP + Gel, and DPP + MOF@Gel were determined by dynamic light scattering using a zeta potential analyzer (Malvern Zetasizer Nano ZS90).

2.13. Release profiles of Cu/GA MOFs

To study Cu/GA MOFs release under varying H_2O_2 concentrations and pH, DPP + MOF@Gel composites containing 125 μg/mL Cu/GA

MOFs were prepared. The composites were immersed in 1 mL solutions of 0, 125, 250, and 500 μM H_2O_2 and in PBS at pH 5.0 and 7.4. At each indicated time point, supernatant absorbance at 260 nm was measured by UV–vis spectrophotometry (Shanghai Meipu UV-3100). Cu/GA MOFs concentration was calculated from the absorbance using a standard curve. The release rate was calculated as: Release rate (%) = Ct/CA × 100 %

Where Ct is the calculated MOF concentration at time t, and CA is the initial MOF loading per DPP. Release curves were generated from the data.

2.14. In vitro cytotoxicity test

The leaching and direct contact methods assessed the cytotoxicity of Cu/GA MOFs and the composite dressings. Sterilized composites were incubated in culture medium for 24 h. L929 and Raw264.7 cells (4 × 10^3 cells/well) were seeded in 96-well plates in regular medium for 24 h. The medium was replaced with 100 μL of leaching solution from Cu/GA MOFs, DPP, DPP + Gel, or DPP + MOF@Gel. At 1, 3, and 7 days, 10 μL CCK-8 reagent in 90 μL medium was added and incubated for 2 h. Absorbance was measured at 450 nm. For direct staining, 2 μM calcein AM and 8 μM propidium iodide in PBS were used. After 1 or 3 days in leaching solutions, L929 and Raw264.7 cells were incubated with the dye (500 μL) for 30 min at 37 °C. Live (green) and dead (red) cells were visualized by inverted fluorescence microscopy. Hemolysis testing was performed by isolating red blood cells (RBCs) from rat whole blood mixed with 109 mM sodium citrate (9:1 ratio). RBCs were centrifuged at 3000 rpm for 5 min and washed with PBS. A 5 % (v/v) RBC suspension was prepared. Composite dressing powder was generated by pulverizing lyophilized samples in liquid nitrogen to obtain a 2.5 mg/mL dispersion. 0.5 mL RBCs were mixed with 0.5 mL of composite dispersions at varying concentrations in 1.5 mL tubes. After incubating at 37 °C for 1 h and centrifuging at 10,000 rpm for 10 min, 200 μL supernatant was transferred to a 96-well plate. Absorbance was measured at 562 nm (Molecular Devices microplate reader). Deionized water and PBS were positive and negative controls. Hemolysis (%) was calculated as: Hemolysis (%) = (Am - Ap)/(Ah - Ap) × 100 %

Where Am is sample absorbance, Ah is water absorbance, and Ap is PBS absorbance. Each concentration was tested in triplicate.

2.15. In vitro cell migration assay

HUVECs were seeded in 6-well plates and cultured in high-glucose DMEM with 10 % FBS. At 90 % confluence, a straight scratch was made through the cell monolayer using a sterile 1 mL pipette tip. Loose cells were washed away with PBS. Cells were then incubated in serum-free DMEM (control) or serum-free DMEM containing sample extracts for 24, 48, and 72 h. Phase contrast images were captured at 0, 24, 48, and 72 h post-scratch. The gap closure rate was quantified using ImageJ software (NIH). In vitro transwell migration assays were performed by suspending HUVECs (1 × 104 cells/pore) in 100 μL DMEM with 1 % FBS. The cells were seeded into 24-well Transwell plates (Corning Inc.) containing Transwell inserts. The lower chambers contained 500 μL of sample extracts (DPP, DPP + Gel, DPP + MOF@Gel) or control medium. After 24 h of incubation at 37 °C and 5 % CO_2, non-migrated cells were removed from the top of the insert using a cotton swab. Migrated cells on the underside were stained with crystal violet (Beyotime) and imaged under a microscope.

2.16. In vitro angiogenesis test

In vitro angiogenesis assays were performed by coating 24-well plates with 300 μL of growth factor reduced Matrigel (BD Biosciences) and incubating at 37 °C for 30 min to solidify. HUVECs (2 × 104 cells/well) were seeded on the Matrigel substrate and treated with sample extracts (DPP, DPP + Gel, DPP + MOF@Gel) in serum-free DMEM or serum-free DMEM only (control). After 6 h of incubation at 37 °C and 5 % CO2, cells were imaged by microscopy (Carl Zeiss) and the number of branch points was quantified using ImageJ software (NIH).

2.17. In vitro antioxidant, ROS elimination, and macrophage polarization tests

The free radical scavenging activity of DPP, DPP + Gel, and DPP + MOF@Gel extracts (containing ~25 μg/mL Cu/GA MOFs) was evaluated by DPPH assay. DPPH (Sigma-Aldrich) was mixed with sample extracts in a 96-well plate (200 μL reaction volume) and incubated in the dark at room temperature for 30 min. Absorbance was read at 517 nm by UV–vis spectroscopy. The percent inhibition was calculated as:

Inhibition (%) = (1 - $OD_{sample}/OD_{control}$) × 100%

ROS elimination by the composite dressings was assessed using DCFH-DA staining. Human dermal fibroblasts and macrophages were treated with sample extracts for 24 h then incubated with 0.3 mM H_2O_2 for 30 min. Cells were stained with 10 μM DCFH-DA in DMEM for 20 min at 37 °C, 5 % CO_2. Fluorescence was imaged by inverted microscopy. Controls lacked extract or H_2O_2 treatment.

Macrophage polarization: Inflammatory microenvironment was formed by adding 100 ng/mL LPS to the culture solution and incubating for 24 h. The cultures were then co-cultured with extract for 48 h. The control group was not treated. Subsequently, 4 % paraformaldehyde was added for cell fixation for 15 min, PBS was rinsed three times for 5 min, then 0.5 % Triton was added for osmotic membrane-breaking treatment for 15 min, and 5 % BSA was added for 2 h of closure. The cells were incubated with rabbit anti-CD206 polyclonal antibody (1:200, Abcam) or rabbit anti-INOS polyclonal antibody (1:200, Abcam) at 4 °C overnight, and goat anti-rabbit IgG H&L (Alexa Fluor® 488) (1:2000, Abcam) or goat anti-rabbit IgG H&L (Alexa Fluor® 594) (1:2000, Abcam) were incubated for 2 h at room temperature. Finally, the nuclei were stained with DAPI and observed and photographed by fluorescence inverted microscope (Leica DMi8).

2.18. In vitro antibacterial test

To evaluate in vitro antibacterial activity, DPP, DPP + Gel, and DPP + MOF@Gel were incubated with *Staphylococcus aureus* or *Escherichia coli* for 12 h. Samples were then fixed overnight in 2.5 % pentanediol, dehydrated through an ethanol gradient, and lyophilized before imaging by SEM. For co-culture assays, dressings were incubated in 24-well plates containing bacterial medium. After incubation, the medium was removed, serially diluted 100,000-fold, and plated using the agar plate method to determine inhibition of *S. aureus* and *E. coli* growth. Plates were imaged and colonies counted after 18 h. Each experimental group was tested in triplicate.

2.19. In vivo wound healing examination

All animal procedures complied with the NIH Guide for the Care and Use of Laboratory Animals and were approved by the Research Ethics Committee of Nanchang University. Infected skin wound healing was evaluated in a rat model. 24 male SD rats (200 ± 20 g, 8 weeks old) were anesthetized and the dorsal area was shaved and disinfected with iodine/ethanol. Full-thickness 8 mm diameter skin defects were generated and infected with 10^7 CFU *Staphylococcus aureus*. Rats were treated with DPP, DPP + Gel, DPP + MOF@Gel, or gauze coverings (negative control). Wound areas were photographed over time to assess healing. On specified days, wound tissue was excised, fixed in 4 % paraformaldehyde, and sectioned. H&E and Masson's trichrome staining evaluated wound healing histologically. The Giemsa stain is used to assess the number of bacteria in the skin tissue. Tissue sections were stained with Giemsa's dye for 15 min, rinsed in distilled water and
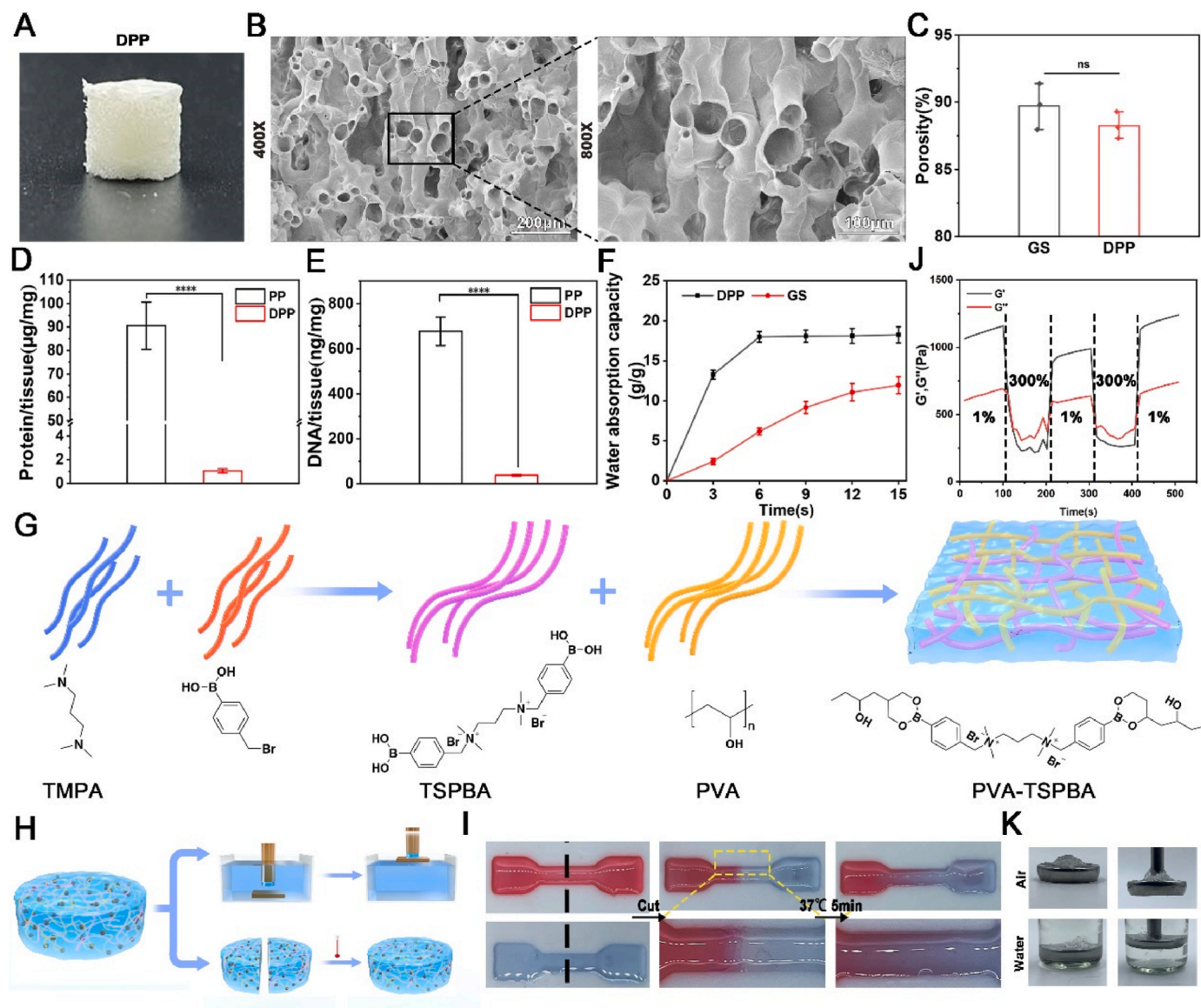
Fig. 1. The preparation and characterization of decellularized pomelo peel (DPP) and PVA-TSPBA hydrogel. (A) The photograph of the DPP. (B) The internal structure of the DPP. (C) The porosity of the DPP and gelatin scaffold (positive control). (D, E) The protein and DNA content of pomelo peel before and after decellularization. (F) The water absorption behavior of the DPP and gelatin scaffold. (G) The schematic illustrates the preparation process of PVA-TSPBA hydrogel. (H) The schematic shows the tests of the self-healing behavior and adhesive capacity of the PVA-TSPBA hydrogel. (I) The self-healing behavior of PVA-TSPBA hydrogel at 37 °C. (J) Dynamic shear rheological characterization of the PVA-TSPBA hydrogels. (K) The adhesive capacity of the PVA-TSPBA hydrogel was identified by the leak test.

visualized under a microscope.

In addition, a rat model was used to evaluate the effect of the composite dressings on scar formation. 24 male SD rats (200 ± 20 g, 8 weeks old) were anesthetized and four 2 cm incisions were made on the shaved and disinfected backs. Rats were treated with sutures (4-0 nonabsorbable), DPP + Gel, DPP + MOF@Gel, or gauze coverings (negative control). Wound areas were photographed over time to assess scab formation, size, and thickness. After 4 and 8 days, skin tissues were excised, fixed in 4 % paraformaldehyde, and sectioned. H&E and Masson's trichrome staining evaluated healing. On day 8, the Vancouver Scar Scale scored re-epithelialization.

2.20. In vivo antibacterial ability evaluation

To establish biofilm-infected wounds, 20 μL of 5×10^7 CFU/mL *Staphylococcus aureus* was applied and allowed to incubate for 1 day. Wound exudate was collected using a swab and cultured on agar plates.

The in vivo antibacterial activity of the dressings was evaluated by counting bacterial colonies. Giemsa staining assessed residual bacteria in the wounds.

2.21. Histological observations

Skin tissue sections were dewaxed and hydrated, followed by antigen repair. After incubation with 10 % goat serum for 30 min at room temperature, CD31 primary antibody (1:100) was added and incubated at 4 °C overnight. After incubation with secondary antibody for 15 min at room temperature, DAB color development was performed. The nuclei were stained with DAPI for 15 min and observed under a fluorescence microscope. Angiogenesis was assessed by CD31 immunofluorescent staining. Relative fluorescence intensity of CD31 was quantified by image analysis and normalized to the blank control group.
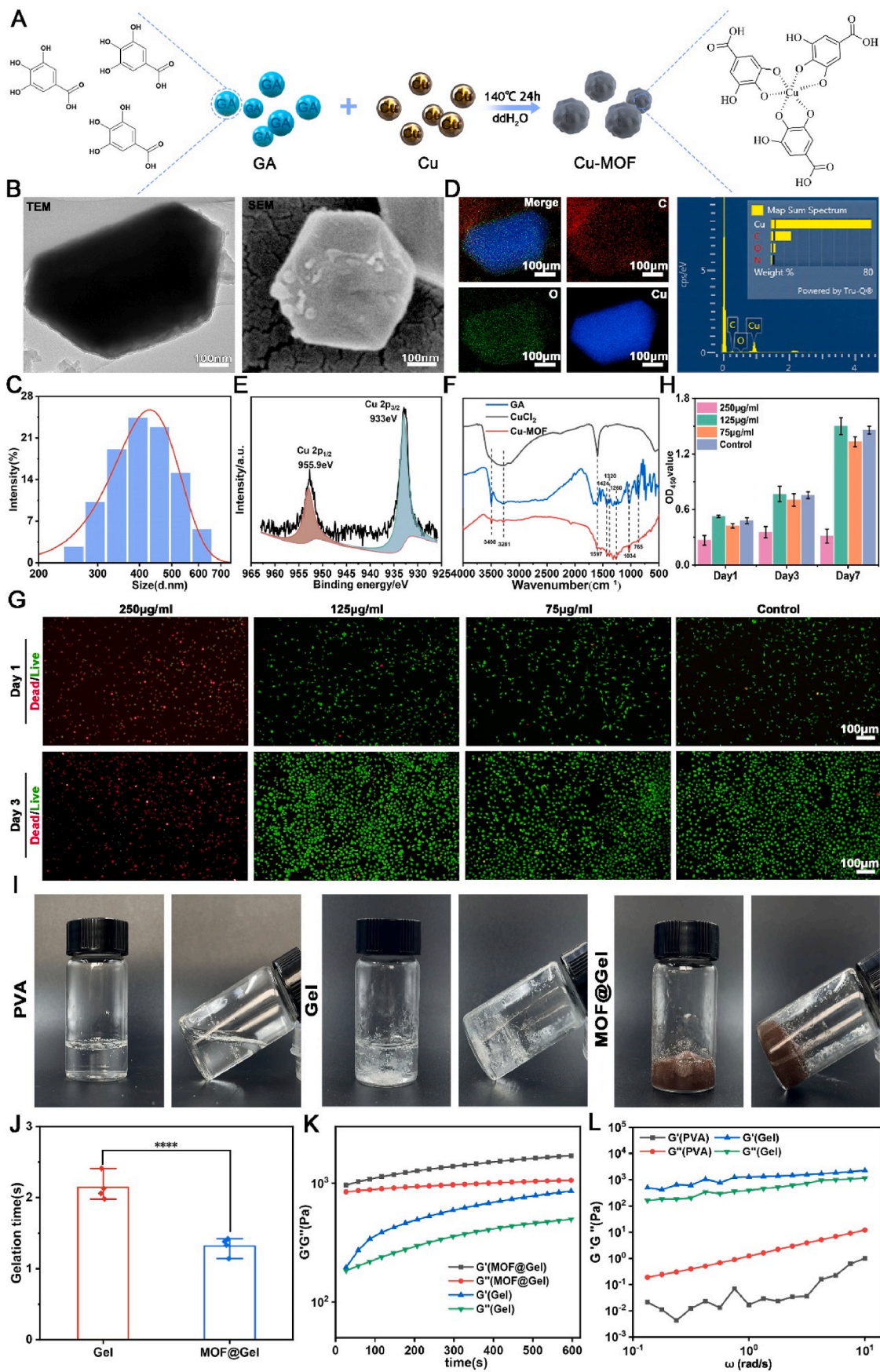
(caption on next page)

Fig. 2. The preparation and characterization of gallic acid/copper MOFs and MOFs loaded PVA-TSPBA hydrogel. (A) The schematic illustrates the preparation process of gallic acid/copper MOFs. (B) TEM and SEM images of gallic acid/copper MOFs. (C) Elemental composition analysis of gallic acid/copper MOFs by energy dispersive X-ray spectroscopy (EDX). (D) The size distribution of gallic acid/copper MOFs particles. (E) Identifying the valency of Cu ion within the gallic acid/copper MOFs. (F) The FTIR characterization of gallic acid, CuCl$_2$, and gallic acid/copper MOFs. (G) The cytotoxicity of gallic acid/Cu^{1+} MOFs with different concentrations on L929 cells after co-cultured with gallic acid/Cu^{1+} MOFs for 1 and 3 days. (H) The quantification of the proliferation of L929 cells after co-cultured with gallic acid/Cu^{1+} MOFs for 1, 3, and 7 days. (I) The photograph of the PVA, PVA-TSPBA, and MOFs loaded PVA-TSPBA hydrogel before and after gelation. (G) The gelation time of the PVA-TSPBA hydrogel and gallic acid/copper MOFs loaded PVA-TSPBA hydrogel. Rheological dynamic time scanning (K) and dynamic frequency scanning (L) of the original hydrogel and MOFs loaded hydrogels.

2.22. Data analysis

Results are expressed as mean $\pm$ standard deviation (SD). Statistical analyses were performed using SPSS 20.0. Graphs were generated in Origin. One-way ANOVA determined statistical significance. P values less than 0.05 were considered significant. P values are denoted as: *p < 0.05, **p < 0.01, ***p < 0.001, ****p < 0.0001.

3. Results and discussion

3.1. Preparation and characterization of DPP and PVA-TSPBA hydrogel

Fig. 1A shows the cylindrical decellularized pomelo peel exhibiting a rough surface morphology. DPP possesses a multi-channel porous architecture, and the porosity of DPP is (88.25 ± 0.58) % which is close to commercial gelatin sponge (89.72 ± 0.99) % (Fig. 1B–C). The elution rate of both DNA and protein of DPP reached more than 95 % (Fig. 1D–E), which meets the standard for decellularized materials. The removal of plant DNA and protein contributes to reduce the immunogenicity of decellularized plant scaffolds [22,23]. Fig. 1F exhibits the water absorption rate of DPP is much faster than gelatin sponge. The DPP can reach maximum water absorption within 6 s, whereas gelatin sponge requires 15 s. Subsequently, we developed hydrogel coating materials to functionalize the DPP. Fig. 1G outlines the synthesis steps for the PVA-TSPBA hydrogel. The N,N-Dimethyl formamide was used as solvent, 4-(bromoethyl)phenylboron and N,N,N,N,N,N-tetramethyl-1, 3-propanediamine (TMPA) were reached at 60 °C for 24 h to obtain TSPBA. And then the TSPBA was mixed with PVA to make PVA-TSPBA hydrogel [24]. We examined the adhesive and self-healing ability of PVA-TSPBA hydrogel (Fig. 1H). As shown in Fig. 1I, the PVA-TSPBA hydrogel could achieve self-healing within 5 min at 37 °C. In addition, the dynamic shear rheological test also proved that the PVA-TSPBA hydrogel has a self-healing ability. The PVA-TSPBA hydrogel is turned into liquids under high shear and reverts to gel states when the shear strain is reduced (Fig. 1J). The underwater adhesion experiments showed that the PVA-TSPBA hydrogel can lift 50 g of iron out of the water by its viscosity (Fig. 1K). Herein, the synthesized PVA-TSPBA hydrogel can enhances the adhesion between the DPP and wound bed, preventing DPP shifting and falling off during application. In addition, the PVA-TSPBA hydrogel contains a lot of water, which can provide moisturization and prevent desiccation and hardening of the DPP.

3.2. Preparation and characterization of gallic acid/Cu MOFs

As shown in Fig. 2A, anhydrous copper chloride and gallic acid powder were fully dissolved in deionized water, then underwent a hydrothermal reaction at 140 °C for 24 h. Strong coordinated interactions between the copper ions and gallic acid ligands formed a unique crystal structure of gallic acid/Cu MOFs with high stability. The TEM and SEM (Fig. 2B) images revealed the synthesized gallic acid/Cu MOF nanoparticles exhibited irregular hexagonal morphologies. Particle size distribution analysis indicated the obtained particles ranged from 300 to 600 nm (Fig. 2C). And the energy mapping scanning analysis showed that the nanoparticles were mainly composed of Cu (79.74 %), C (14.31 %), O (4.58 %) (Fig. 2D). Moreover, the main peaks of Cu 2p$_{3/2}$ at 933 eV and Cu 2p$_{1/2}$ at 955.9 eV, and a very weak satellite peak at 945 eV (Fig. 2E). For one thing, there is no typical +2 state Cu satellite peaks at

940 and 962 eV [25]. For another, the ligand gallic acid has strong reducing properties, it is capable of reducing divalent copper to monovalent copper [26,27]. Thus, we speculate that we have prepared monovalent copper MOFs in this study. The FTIR spectra showed that the wave peaks of gallic acid/Cu MOFs cover the major wave peaks of Cu and gallic acid (Fig. 2F). Copper ions also have cytotoxicity issues [28], so we examined the cytotoxicity of gallic acid/Cu MOFs in vitro. As shown in Fig. 2G and **H**, high concentrations of MOFs (250 µg/mL) can cause massive L929 cell death after co-culture for 1 and 3 days, respectively. In contrast, no significant cell death was observed in the groups treated with lower MOF concentrations of 125 µg/mL and 75 µg/mL (Fig. 2G and H). Then, gallic acid/Cu MOFs were mixed with PVA-TSPBA hydrogel to enhance the function of hydrogel, and the final concentration of gallic acid/Cu MOFs was 125 µg/mL. Herein, to reduce the cytotoxicity of copper ions, the effective way is to control its concentration below 125 µg/mL according to our results. As shown in Fig. 2I, the PVA couldn't gelation without any treatment. The PVA-TSPBA (Gel) and MOFs loaded hydrogel (MOF@Gel) mixtures formed hydrogel. The gelation time of MOF@Gel (1.32 ± 0.12) s was much shorter than that of Gel (2.15 ± 0.19) s (Fig. 2J). We speculate that the copper ion/gallic acid MOFs contain more hydroxyl groups, and the hydrogen bonding interactions further shorten the gelation time. The rheological dynamic time scanning (Fig. 2L) and dynamic frequency scanning (Fig. 2K) demonstrated that PVA was in the liquid state with G'' > G', whereas PVA-TSPBA was in the gel state with G' > G ''.

3.3. Preparation and characterization of functionalized DPP coated with gallic acid/copper MOFs loaded PVA-TSPBA hydrogel (DPP + MOF@Gel)

As shown in Fig. 3A, the schematic shows the composition of DPP + MOF@Gel, comprising DPP, PVA-TSPBA hydrogel, and gallic acid/Cu MOFs. In this system, DPP acts as the substrate material. The PVA-TSPBA hydrogel functions as a coating to enhance DPP's adhesive and moisture retention ability [13]. Meanwhile, the gallic acid/Cu MOFs provide antibacterial activity [29]. The interface between the DPP and hydrogel shows the DPP was coated entirely with a thin, ~200 µm layer of hydrogel (Fig. 3B). Surface images of DPP + MOF@Gel exhibited that the hydrogel coating did not obstruct the DPP's underlying porous architecture and rough topography (Fig. 3C). The energy spectroscopy analysis showed that the DPP sponge was predominantly composed of C (57.9 %) and O (42.1 %) elements. The MOF@Gel primarily contained C (41.4 %), Cu (40.8 %) and O (17.8 %), while the DPP + MOF@Gel was composed of C (45.6 %), Cu (33.1 %) and O (21.3 %) (Fig. 3D). The compressive stress of DPP + MOF@Gel $(4.53 \pm 0.14$ MPa) was much greater than DPP $(3.59 \pm 0.09$ MPa) and MOF@Gel$(0.28\pm; 0.03$ MPa) with 90 % compressive strain (Fig. 3E). The tensile stress of DPP + MOF@Gel before fracture can reach 337.52 ± 7.54 KPa, which is much higher than DPP $(299.03 \pm 10.23$ KPa) (Fig. 3F). The compressive and tensile properties of the DPP material ensure its structural integrity even under a certain external force stimulus during use [30,31]. The adhesive strength of DPP + Gel and DPP + MOF@Gel on glass were (138.71 ± 7.12) KPa and (145.24 ± 11.48) KPa, and on porcine skin it was (181.67 ± 10.15) KPa and (190.67 ± 6.36) KPa (Fig. 3G, **H**). Fig. 3I further visualized the strong adhesive ability of DPP + MOF@Gel, which could block the leaking water. The gallic acid and copper ions showed a boost release under acidic condition (pH 5.0), while showed a slowly and
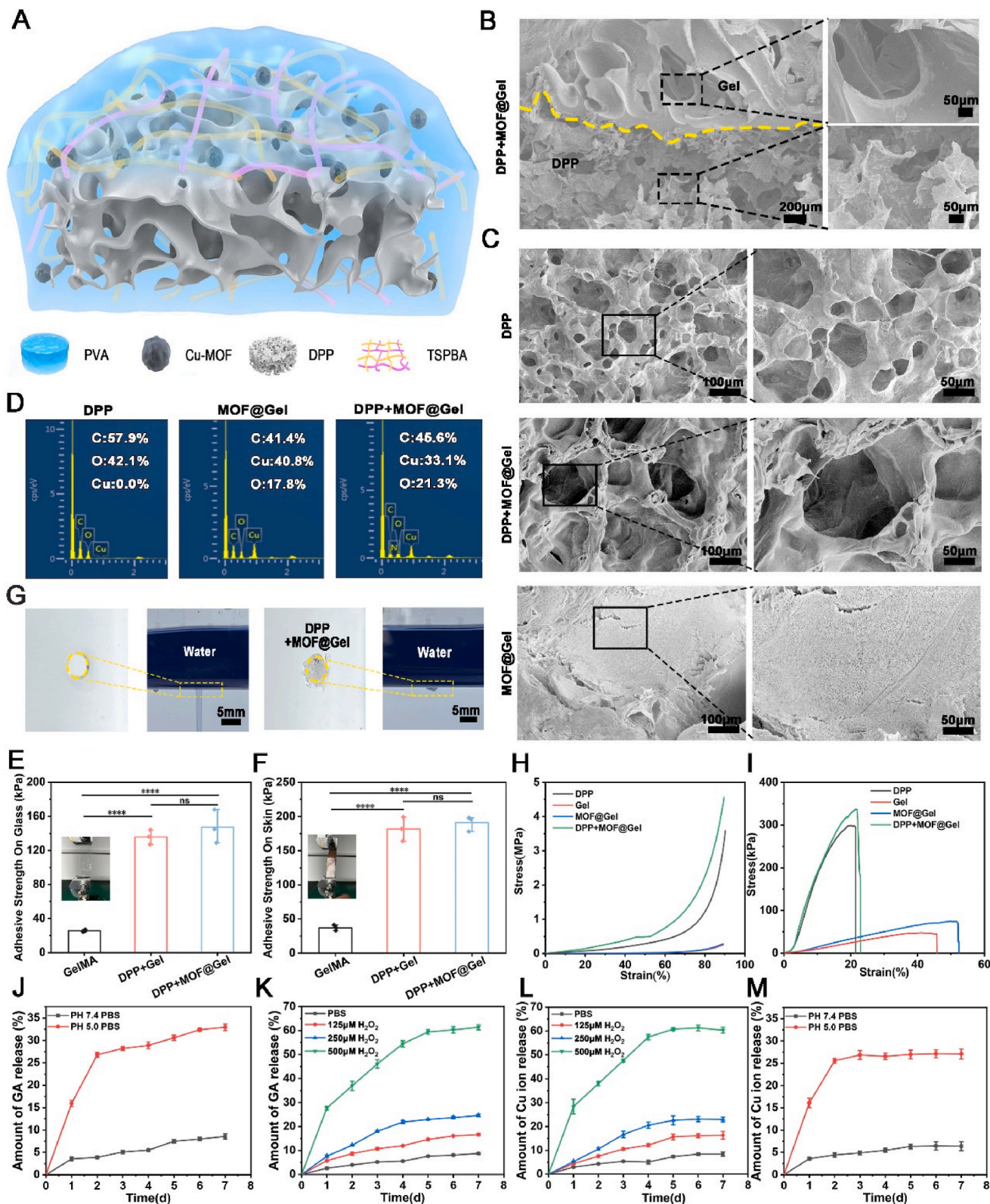
Fig. 3. The preparation and characterization of functionalized DPP coated with gallic acid/copper MOFs loaded PVA-TSPBA hydrogel (DPP + MOF@Gel).
(A)The schematic illustrates the composition of the DPP + MOF@Gel. (B) The cross-section shows the interface between DPP and a thin layer of hydrogel. (C) The morphology of DPP, MOFs@Gel, and DPP + MOF@Gel. (D) The elemental analysis of DPP, MOFs@Gel, and DPP + MOF@Gel. (E, F) The adhesive capacity of the GelMA, DPP + Gel, and DPP + MOF@Gel on glass (H) and skin (I). (G) The adhesive capacity of DPP + MOF@Gel was identified by the leak test. (H, I) The Compressive (H) and tensile (I) properties of DPP, Gel, MOF@Gel, and DPP + MOF@Gel. (J) The release profile of gallic acid from DPP + MOF@Gel under pH 7.4 and pH 5.0 PBS solution. (K) The release profile of gallic acid from DPP + MOF@Gel in 0, 125, 250, and 500 μm H_2O_2 PBS solution. (L) The release profile of copper ion from DPP + MOF@Gel in 0, 125, 250, and 500 μm H_2O_2 PBS solution. (M) The release profile of copper ion from DPP + MOF@Gel under pH 7.4 and pH 5.0 PBS solution.
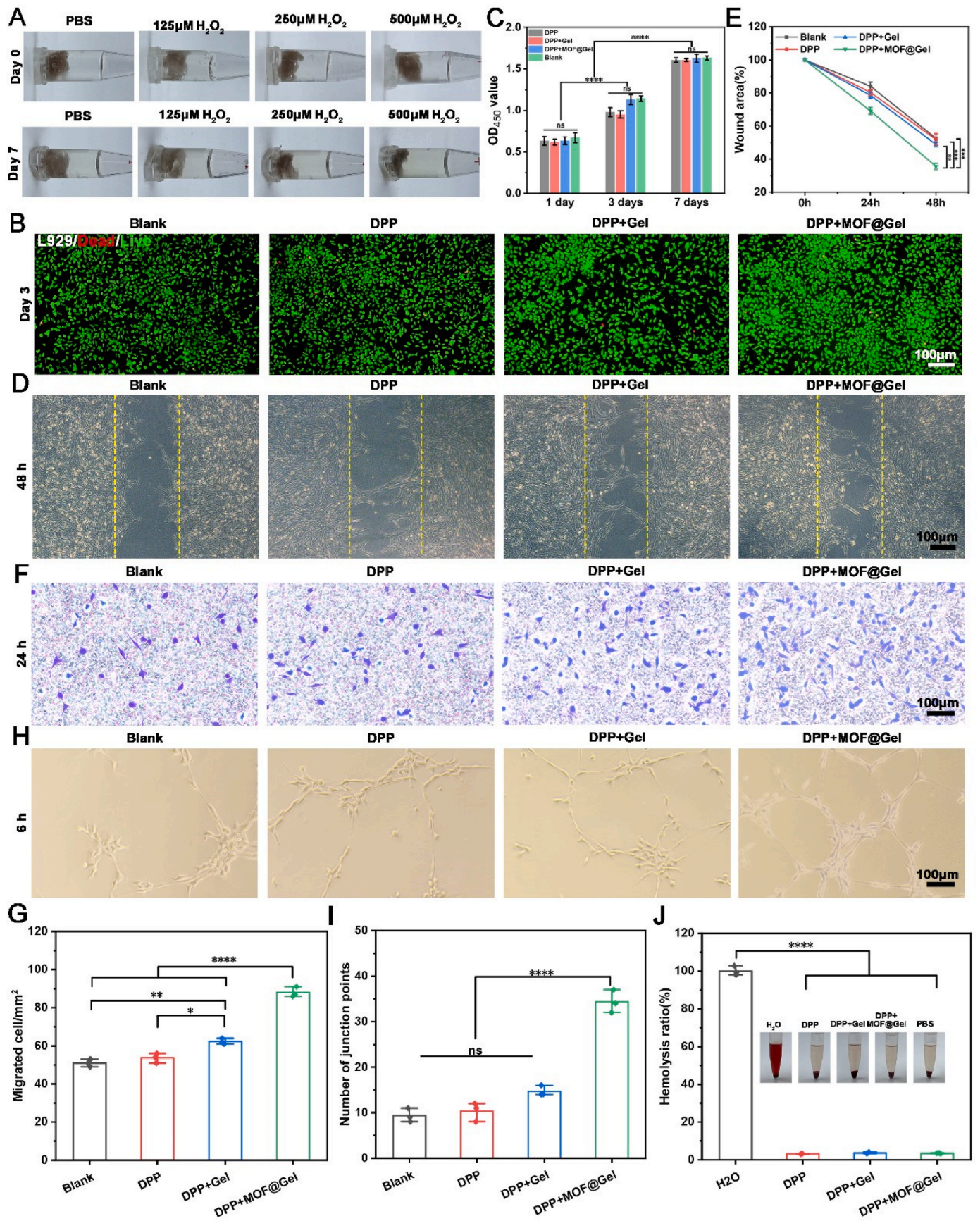
(caption on next page)

Fig. 4. The biocompatibility test of DPP + MOF@Gel. (A) The morphology of the DPP + MOF@Gel after 7 days of degradation at different concentrations of H_2O_2. (B) Live/Dead assay of L929 cells treated with DPP, DPP + Gel, and DPP + MOF@Gel extracts after 1 and 3 days of culture. (C) The proliferation of L929 cells treated with the extracts of DPP, DPP + Gel, and DPP + MOF@Gel for 1, 3, and 7 days, respectively. (D) The scratch assay of L929 cells treated the extracts of DPP, DPP + Gel, and DPP + MOF@Gel for 24 and 48 h. (E) The quantification of the residual wound of DPP, DPP + Gel, and DPP + MOF@Gel groups after 24 and 48 h of migration. (F) The transwell assay of L929 cells treated the extracts of DPP, DPP + Gel, and DPP + MOF@Gel for 24 h. (G) The quantification of the infiltrated L929 cells of DPP, DPP + Gel, and DPP + MOF@Gel groups after 24 h of migration. (H) The tubular formation assay of HUVECs treated the extracts of DPP, DPP + Gel, and DPP + MOF@Gel for 24 h. (I) The quantification of junction points of the formed tubular in DPP, DPP + Gel, and DPP + MOF@Gel groups. (J) Hemolysis test of DPP, DPP + Gel, DPP + MOF@Gel.

sustained release under physiological condition (pH 7.4). In addition, the release of gallic acid and copper ions would be accelerated with the increased concentration of H_2O_2 from 125 to 500 μm (Fig. 3J-**3M**). The initial rapid release of copper ions can kill most bacteria quickly and control the progress of wound infection [29].

3.4. The biocompatibility examination of DPP + MOF@Gel

In the microenvironment of chronic wounds, the activities of various enzymes are impaired [32]. However, large amount of ROS exist in the microenvironment of the chronic wound which can affect the degradation of materials [33]. Therefore, we examined the degradation of DPP + MOF@Gel under different concentrations of H_2O_2. As shown in Fig. 4A and Figure S1, the DPP + MOF@Gel could gradually degrade in the presence of H_2O_2, and the degradation rate of the DPP + MOF@Gel could be accelerated with the increased concentration of H_2O_2. We also explored the cytotoxicity of DPP + MOF@Gel. The extracts of DPP, MOF@Gel, and DPP + MOF@Gel did not affect the proliferation of L929 cells and RAW264.7 cells after co-culture for 1, 3 and 7 days (Fig. 4B and C and Figure S2). Following, we explored the effects of DPP + MOF@Gel on cell migration. As shown in Fig. 4D, E and Figure S3, the fastest wound healing was observed in the DPP + MOF@Gel group compared to the DPP and DPP + Gel groups. In addition, the transwell assay revealed that the DPP + MOF@Gel group had more infiltrated cells (88 ± 3 cells/mm^2) compared to the DPP + Gel group (62 ± 2 cells/mm^2), DPP group (54 ± 3 cells/mm^2), and blank group (51 ± 2 cell/mm^2) (Fig. 4F and **G**). Yang et al. demonstrated that gallic acid could accelerate keratinocyte and fibroblast migration by activating focal adhesion kinases (FAK) under both normal and high-glucose conditions [34]. Moreover, HUVECs treated with DPP + MOF@Gel extracts exhibited obvious tubular formation compared to the other 3 groups. The average numbers of formed nodes in the DPP + MOF@Gel group (34 ± 3) were significantly more than the DPP + Gel (15 ± 1), DPP (10 ± 2), and blank groups (9 ± 2) groups (Fig. 4H and I). Finally, there was no significant hemolysis among the dispersions of the DPP, DPP + Gel, and DPP + MOF@Gel (Fig. 4J).

3.5. In vitro analysis of antibacterial capacity, antioxidant capacity and macrophage polarization capacity of DPP + MOF@Gel

As shown in Fig. 5A, the colony formation exhibited that DPP + MOF@Gel had strong antimicrobial capacity. The survival rates of E. coli and S. aureus in the DPP + MOF@Gel treated group were (9.09 ± 0.48)% and (9.90 ± 1.47)%, respectively. These were significantly lower compared to 87.84 ± 2.33 % (E. coli) and 90.50 ± 1.19 % (S. aureus) for DPP + Gel, and 97.26 ± 1.78 % (E. coli) and 98.07 ± 1.82 % (S. aureus) for DPP (Fig. 5B and **C**). The SEM images directly discovered that E. coli and S. aureus could survive on the surface of DPP and DPP + Gel groups, and keep their original shape after 24 h of co-culture. In contrast, E. coli and S. aureus cultured on DPP + MOF@Gel appeared non-viable, with collapsed cellular architecture after 24 h (Fig. 5D). In this study, the antibacterial activity of DPP + MOF@Gel is derived from copper ions. Many studies have confirmed the antibacterial effect of copper ions. For example, Sun et al. developed a multifunctional chitosan-copper-gallic acid based antibacterial nanocomposite wound dressing. The Cu nanoparticles and Cu ions showed strong antibacterial properties [35]. Following, we also explored the ROS

scavenging ability of DPP + MOF@Gel. The 2′,7′-dichlorodihydrofluorescein diacetate (DCFH-DA) was used as a ROS probe, the green fluorescence intensity was used to evaluate ROS levels. As shown in Fig. 5E, the fluorescence intensity was significantly reduced in the DPP + MOF@Gel group compared to the blank, DPP, and DPP + Gel groups after H_2O_2 stimulation. In addition, the inhibitory effect of DPP + MOF@Gel (61.10 ± 1.73 %) on free radicals was significantly stronger than DPP (5.16 ± 1.05 %) and DPP + Gel (6.41 ± 1.16 %) groups (Fig. 5F). Finally, we detected the effects of DPP + MOF@Gel on macrophage polarization. LPS-induced inflammation in RAW264.7 cells led to predominant M1 macrophage polarization, indicated by high iNOS$^+$ expression, in blank, DPP, and DPP + Gel groups. On the contrary, the RAW264.7 cells treated with DPP + MOF@Gel extracts exhibited increased CD206 expression and M2 macrophage polarization (Fig. 5G). For one thing, the PVA-TSPBA hydrogel contains chemical groups capable of reacting with ROS, resulting in clearing the ROS produced in the tissue microenvironment [13,36]. For another, the DPP contains compounds such as pectin, polysaccharides, phenolic acids, flavonoids, coumarins, carotenoids, and aroma-active volatiles [3]. These compounds have been identified to have anti-inflammatory, antioxidant and other properties [4,37]. Therefore, the DPP + MOF@Gel combined the inherent anti-inflammatory, anti-oxidiant, ROS scavenging functions of DPP and PVA-TSPBA hydrogel. And the exertion of these functions is also conducive to the polarization of M2 macrophages.

3.6. The effects of DPP + MOF@Gel on bacteria-infected skin wound healing

As shown in Fig. 6A, DPP, DPP + Gel, and DPP + MOF@Gel dressings were applied to S. aureus-infected skin defect. Wound photography revealed accelerated wound closure in the DPP + MOF@Gel group compared to other groups. For example, the residual wound area of the DPP + MOF@Gel group (28.69 ± 0.59 %) was much smaller than the DPP (52.67 ± 2.63 %), DPP + Gel (43.49 ± 1.95 %), and the blank groups (73.17 ± 1.15 %) after 3 days of treatment (Fig. 6B). Subsequently, we examined the in vivo antibacterial efficacy of DPP + MOF@Gel post-application. As shown in Fig. 6C, the S. aureus survival rate of the DPP + MOF@Gel group was only 7.09 ± 1.87 % after 3 days of treatment, which was significantly decreased compared to DPP (93.92 ± 2.88 %), DPP + Gel (87.75 ± 3.95 %) (Fig. 6D). Furthermore, Giemsa staining revealed abundant S. aureus within the wound tissues of Control, DPP, and DPP + Gel groups on both day 3 and day 7 (Fig. 6E). On the contrary, only a few residual S. aureus were found in the DPP + MOF@Gel treated group on both day 3 and day 7. Especially on day 7, the wound is almost bacteria-free (Fig. 6F). The good antibacterial effect of DPP + MOF@Gel is attributed to copper ions. It has been discovered that the positively charged copper ions combine with negatively charged bacteria, and copper ions can destroy the cell wall when they enter the bacteria, resulting in the death of the bacteria. In addition, the copper ions entering the cells can interact with the protein enzymes of bacteria. It acts to denature and inactivate enzymes, thereby killing bacteria [29, 35].

Human skin tissue defects are primarily repaired by in situ growth of granulation tissue, which consists of infiltrating cells, neovascularization, and newly synthesized extracellular matrix [38,39]. As shown in Fig. 7A, more granulation formation was observed in the DPP, DPP + Gel, and DPP + MOF@Gel groups compared to the control group.
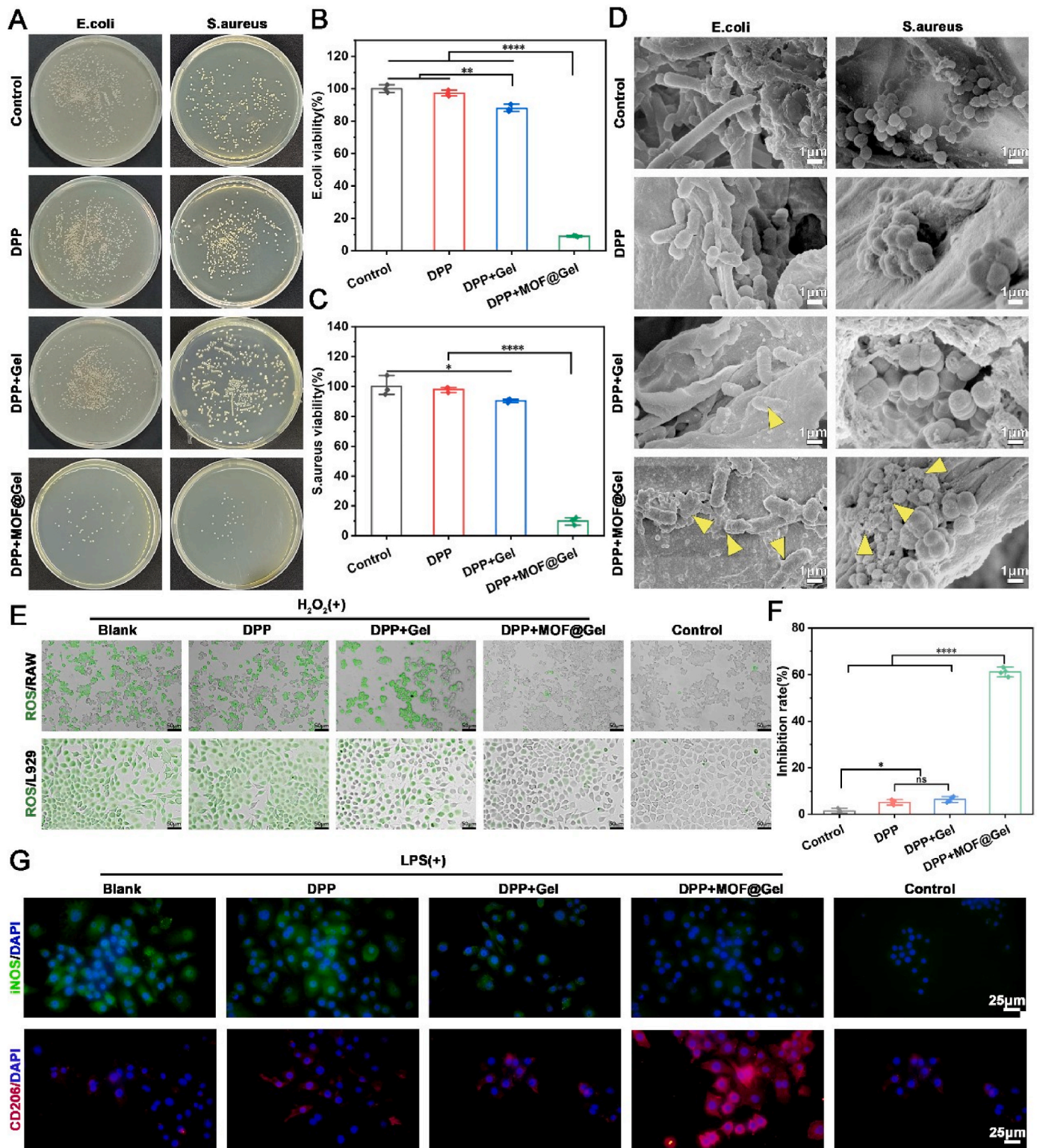
Fig. 5. In vitro antibacterial, ROS clearance, anti-oxidant, and macrophage polarization tests of DPP + MOF@Gel. (A) The colony formation of the *E. coli* and *S. aureus* after treatment with the extracts of DPP, DPP + Gel, and DPP + MOF@Gel for 24 h. The quantification of the *E. coli* (B) and *S. aureus* (C) inhibition ratio of (A). (D) The morphology of *E. coli* and *S. aureus* cultured on the surface of DPP, DPP + Gel, and DPP + MOF@Gel for 24 h. (E) The ROS clearance ability of the extracts of DPP, DPP + Gel, and DPP + MOF@Gel on H₂O₂ pretreated L929 cells and RAW cells. (F) The anti-oxidant ability of the extracts of DPP, DPP + Gel, and DPP + MOF@Gel. (G) The effects of the DPP, DPP + Gel, and DPP + MOF@Gel extracts on macrophage polarization.
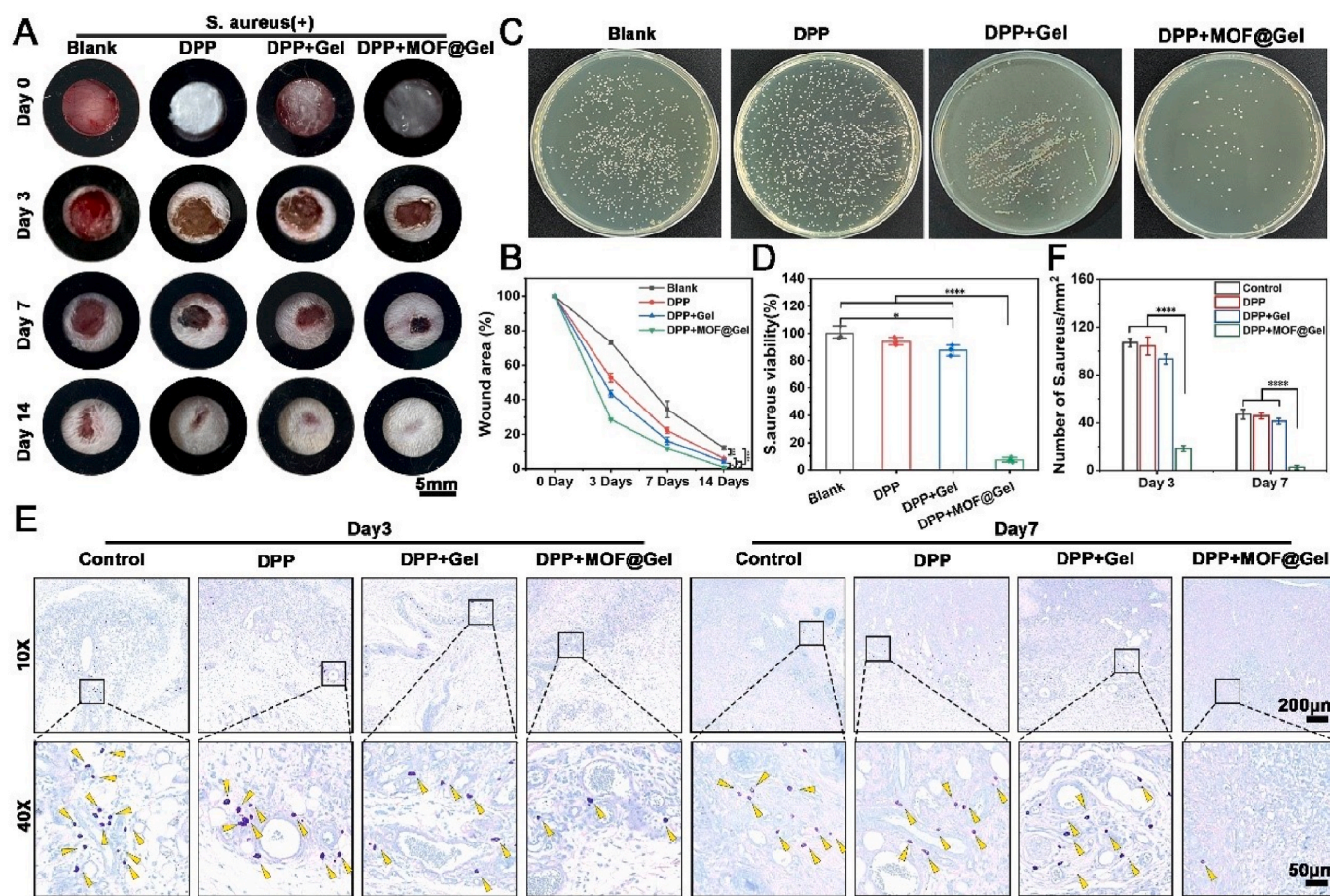
Fig. 6. The effects of DPP + MOF@Gel on biofilm infected skin wound healing. (A) The photographs of the wounds treated with DPP, DPP + Gel, and DPP + MOF@Gel for 3, 7, and 14 days respectively. (B) The residual wound area of DPP, DPP + Gel, and DPP + MOF@Gel groups at each indicated time point. (C) The colony formation of *S. aureus* derived from the wounds treated with DPP, DPP + Gel, and DPP + MOF@Gel for 3 days. (D) The *S. aureus* viability of DPP, DPP + Gel, DPP + MOF@Gel on day 3. (E) The Giemsa staining of DPP, DPP + Gel, and DPP + MOF@Gel groups after 3 and 7 days of treatment. (F) The quantification of detected *S. aureus* within the wound area of DPP, DPP + Gel, and DPP + MOF@Gel groups after 3 and 7 days of treatment.

And the thickness of granulation tissue in the DPP + MOF@Gel group (270.33 ± 7.09)μm reached a peak level at day 7, which was much thicker than the DPP + Gel (170.67 ± 13.57)μm, DPP (136 ± 5.57)μm, and blank group (104 ± 6.56)μm (Fig. 7C). Moreover, the DPP + MOF@Gel group exhibited increased CD31 positive cells within granulation tissue compared to the DPP + Gel, DPP, and blank groups after 7 and 14 days of treatment (Figure S4). Besides, the re-epithelialization rate of the DPP + MOF@Gel group had reached (80.18 ± 1.46)% on day 14, which was much higher than the DPP (56.72 ± 1.22)%, DPP + Gel (65.08 ± 1.72)% and blank group (49.76 ± 1.19)% (Fig. 7B). Additionally, a large amount of collagen deposition was seen in the DPP + MOF@Gel (70.76 ± 1.43 %) and DPP + Gel (63.27 ± 1.64 %) groups compared to the DPP (53.06 ± 1.23 %) and blank groups (48.09 ± 1.93 %) (Fig. 7E). Furthermore, numerous regenerated hair follicles were present in the wound center of the DPP + MOF@Gel group, while limited hair follicle regeneration occurred in the other three groups. The regeneration of hair follicle and other skin appendages helps to reduce scarring and improve healing quality [40,41].

Finally, we explored the immune responses during wound healing. The expression of iNOS$^+$ (M1 macrophage) in the DPP + MOF@Gel group was lower than DPP + Gel, DPP, and control groups on both day 3 and day 7 (Fig. 8A and B). And the expression of CD206 (M2 macrophage) in the DPP + MOF@Gel group was dramatically increased than DPP + Gel, DPP, and control groups on both day 3 and day 7 (Fig. 8A and C). In addition, the ratio of M1/M2 macrophages revealed that the inflammatory status of DPP + MOF@Gel, DPP + MOF@Gel, and DPP

groups all belong to pro-regenerative status on day 3 and day 7. Especially on day 7, the ratio of M1/M2 macrophages of the DPP + MOF@Gel group (0.12 ± 0.02) was much lower than DPP + Gel (0.42 ± 0.03), DPP (0.58 ± 0.04), which was less than 1 (Fig. 8D). In vitro, we have already demonstrated the DPP + MOF@Gel could promote M2 macrophage polarization. The in vivo results further verify this result. This DPP + MOF@Gel regulated local immune responses from pro-inflammatory status to pro-regenerative status, and provide a good wound bed for wound healing.

3.7. The wound-suturing ability of DPP + MOF@Gel

In the preceding wound healing experiment, we observed the smallest scar area with DPP + MOF@Gel treatment. We conducted wound suturing experiments with professional scar assessment to further validate these findings. As shown in Fig. 9A, the DPP + Gel and DPP + MOF@Gel dressings were placed over the incisions, and the incisions were closed directly with sutures or kept opening as controls. The incisions treated with suture and DPP + Gel had not fully closed on day 4. And the incision treated with suture still had a scab on day 8, while the DPP + MOF@Gel group had no visible scar formation (Fig. 9A and B). The quantitative analysis further revealed that the final scar area of DPP + MOF@Gel group (3.87 ± 1.56 %) was significantly low than the suture (3.87 ± 1.56 %) and DPP + Gel group (3.87 ± 1.56 %) (Fig. 9C). Moreover, the Vancouver Scar Scale was used to evaluate the formed scar in different groups [42], and the DPP + MOF@Gel group had the
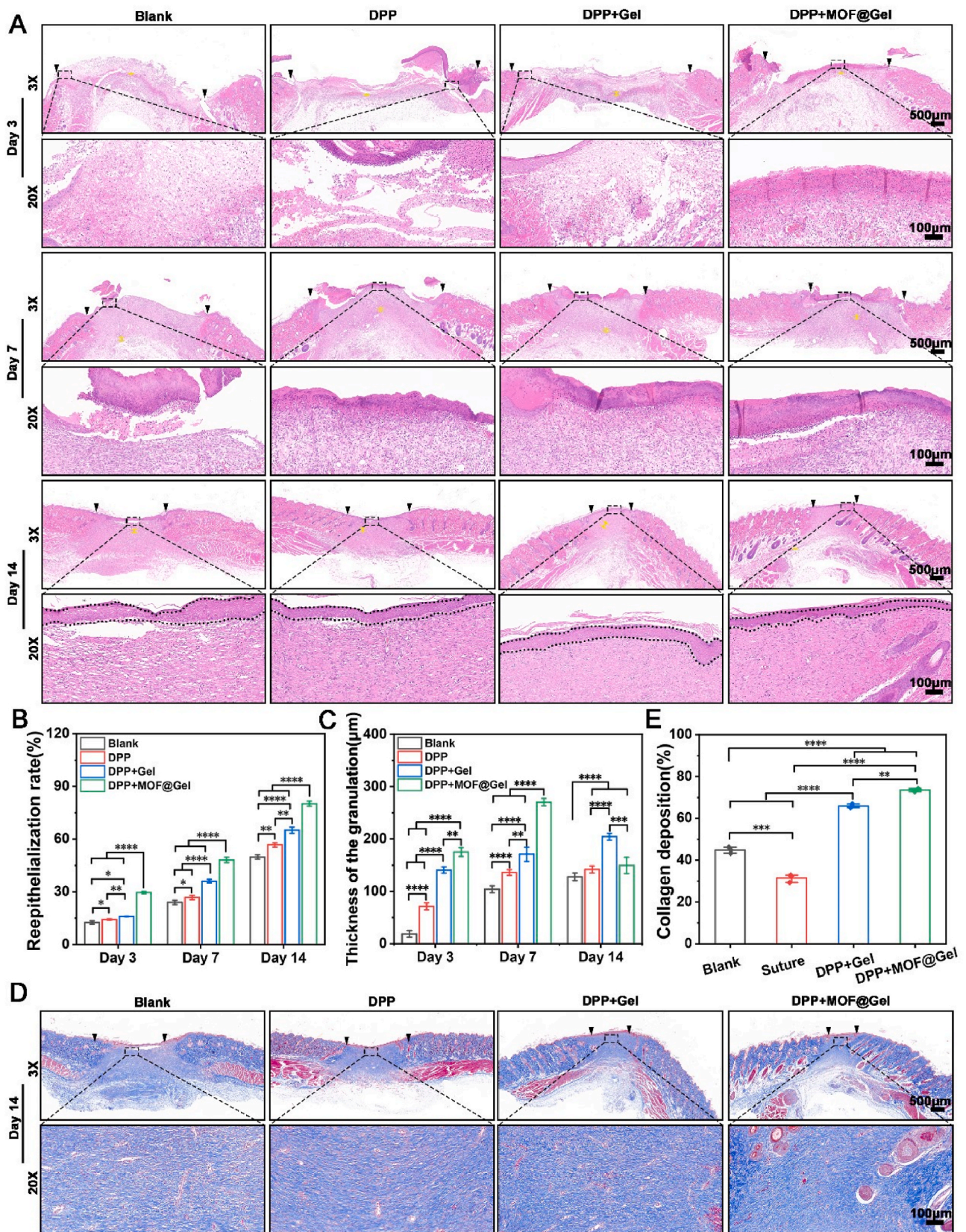
Fig. 7. Histological observations. (A) The HE staining of DPP, DPP + Gel, and DPP + MOF@Gel groups after 3, 7, and 14 days of treatment. (B) The quantification of re-epithelialization rate of DPP, DPP + Gel, and DPP + MOF@Gel on day 3, 7, and 14, respectively. (C) The thickness of the granulation of the wound area within DPP, DPP + Gel, and DPP + MOF@Gel groups on day 3, 7, and 14, respectively. (D) The trichrome staining of the wound center area of DPP, DPP + Gel, and DPP + MOF@Gel groups after 14 days of treatment. (E) The collagen deposition of wound center area of DPP, DPP + Gel, DPP + MOF@Gel group after 14 days of treatment.
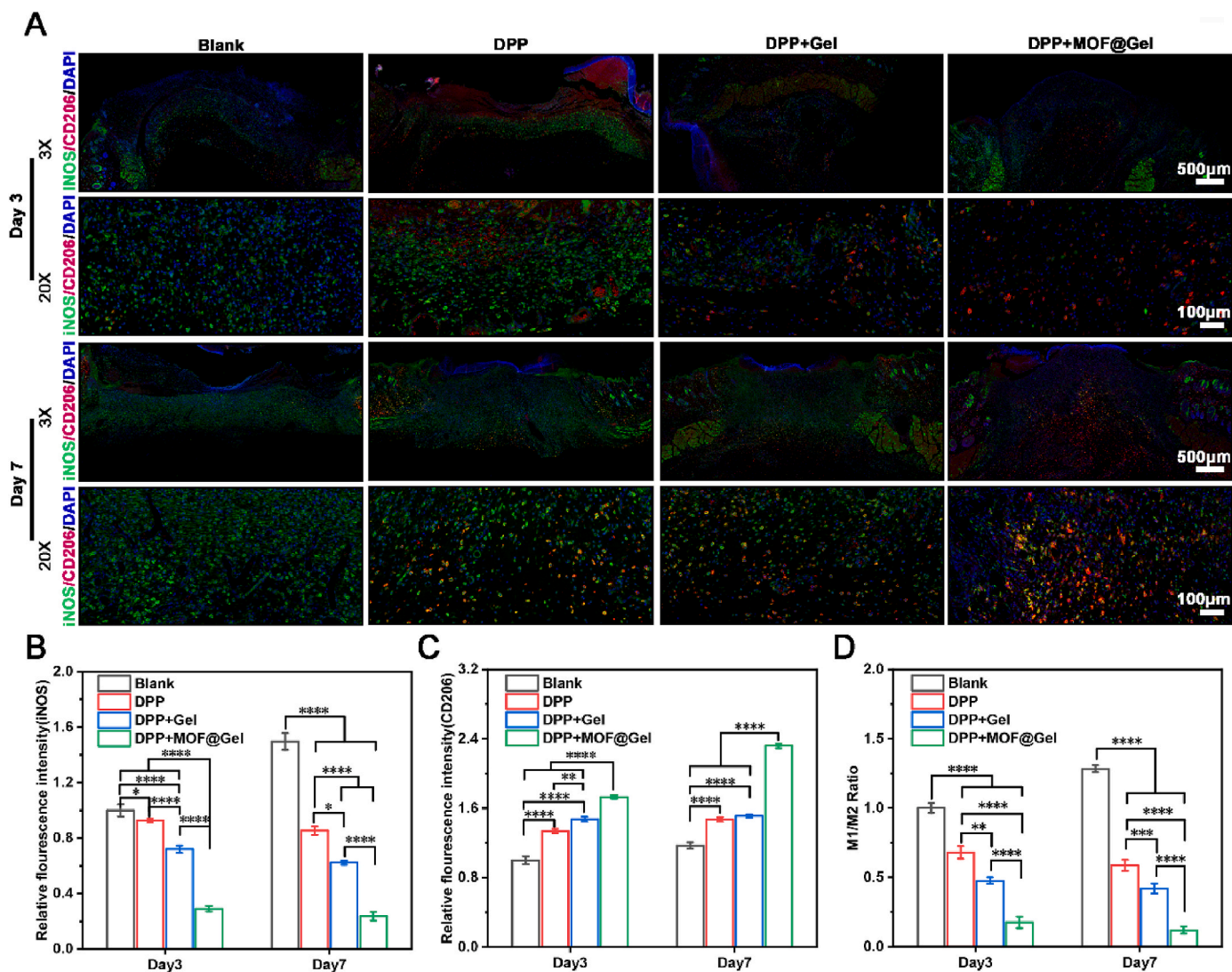
Fig. 8. **The inflammatory responses of DPP + MOF@Gel during wound healing**. (A) The co-staining of CD206 (M2 macrophage) and iNOS$^+$ (M1 macrophage) of DPP, DPP + Gel, DPP + MOF@Gel group after 3 and 7 days of treatment. (B) The relative fluorescence intensity of iNOS expression on day 3 and 7, respectively. (C) The relative fluorescence intensity of CD206 expression on day 3 and 7, respectively. (D) The ratio of numbers of iNOS positive cells/numbers of CD206 positive cells on day 3 and day 7.

lowest score close to normal skin (Fig. 9D). The HE staining results further discovered that the DPP + MOF@Gel treated incision was completely healed on day 4, and many hair follicles (yellow stars) were presented at the incision site on day 8 (Fig. 9E). Trichrome staining showed a prominent scar area and less collagen deposition in the blank, suture, and DPP + Gel groups. In contrast, the DPP + MOF@Gel group had an obvious scar area, and collagen orientation was close to the normal skin (Fig. 9F).

Inflammation is a major cause of hypertrophic scar formation. Appropriate suppression of the pro-inflammatory response during skin wound repair can greatly reduce scar formation after wound healing. Liu et al. developed a biomedical blue by using lipoic acid, which can decreasing the expression of inflammatory cytokines and transforming growth factor-β1 (TGF-β1), resulting in scarless wound healing [43]. Reactive oxygen species Scavenging is feasible as another target to reduce scar formation. Carney et al. reported over 25 ROS scavenger genes significantly downregulated in the hypertrophic scar at all time points compared with basal level controls in a swine wound healing model [44]. In our study, the DPP + MOF@Gel exhibited good anti-inflammatory, anti-oxidant, ROS scavenging functions. This may be the main reason for reducing scar formation of DPP + MOF@Gel.

4. Conclusion

In this study, the decellularized pomelo peel (DPP) coated with gallic acid/copper MOFs loaded PVA-TSPBA hydrogel (DPP + MOF@Gel) was developed for bacteria-infected wound healing and stitching wound. In this hybrid wound dressing, the DPP is the substrate material. The PVA-TSPBA hydrogel works as a coating material to enhance DPP's adhesive and moisture retention ability. The gallic acid/Cu MOFs are antibacterial agents. In vitro, the DPP + MOF@Gel exhibits good biocompatibility. For example, it does not affect the proliferation of fibroblast cells and immune cells, and it can promote the migration of fibroblasts and the angiogenesis of endothelial cells. In addition, it also can scavenge ROS, anti-oxidant, and promote M2 macrophage polarization. Moreover, the DPP + MOF@Gel is capable of inhibiting the viability of *S. aureus* and *E. coli* both in vitro and in vivo. The histological observations revealed that the granulation tissue formation, re-epithelialization, and angiogenesis were also significantly enhanced in the DPP + MOF@Gel group. And the local immune responses had changed from a pro-inflammatory to a pro-regenerative state in the DPP + MOF@Gel group. The skin incision stitching experiment further exhibits DPP + MOF@Gel could reduce scar formation during wound
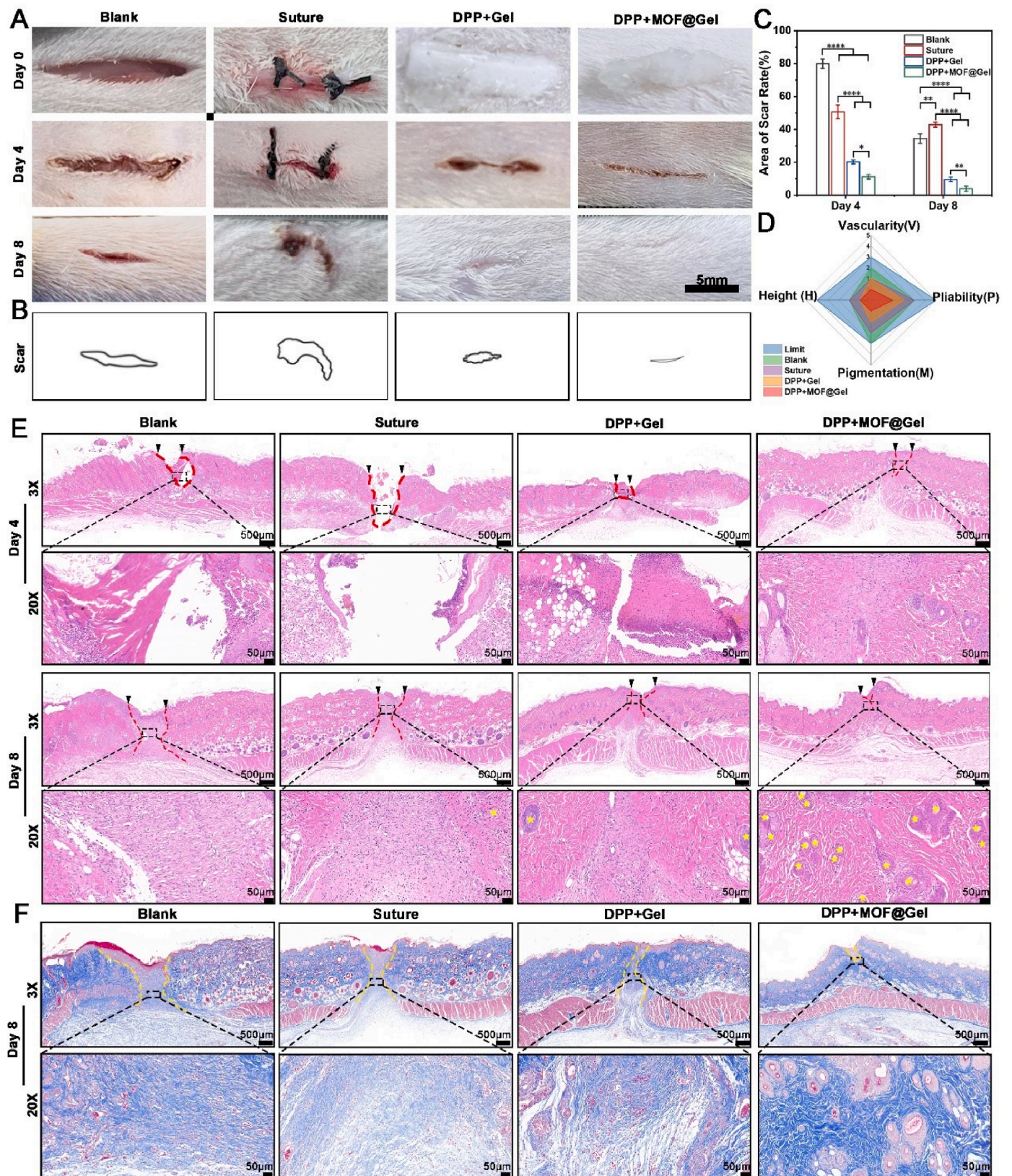
Fig. 9. The wound-suturing ability of DPP + MOF@Gel. (A) The photographs of wound-suturing tests of suture, DPP + Gel, and DPP + MOF@Gel after 4 and 8 days of treatment. (B) The visualization of the formed scar of suture, DPP + Gel, and DPP + MOF@Gel groups after 8 days of treatment. (C) The scar area of DPP + Gel, and DPP + MOF@Gel groups after 8 days of treatment. (D) The Vancouver scar score of DPP + Gel, and DPP + MOF@Gel groups after 8 days of treatment. The H&E (E) and trichrome staining (F) of the wound area of DPP + Gel, and DPP + MOF@Gel groups after 4 and 8 days of treatment.

healing. These results suggest the hybrid DPP + MOF@Gel may provide a new method for managing biofilm-infected skin wounds.

Data availability

Data will be made available on request.

Declaration of competing interest

All authors declare no competing interests.

Acknowledgments

Appendix A. Supplementary data

Supplementary data to this article can be found online at https://doi.org/10.1016/j.bioactmat.2023.10.005.

References

[1] K.-F. Huang, Y.-C. Hsu, C.-N. Lin, J.-I. Tzeng, Y.-W. Chen, J.-J. Wang, Shiunko promotes epithelization of wounded skin, Am. J. Chin. Med. 32 (3) (2004) 389–396.

[2] K.-F. Chak, C.-Y. Hsiao, T.-Y. Chen, A study of the effect of shiunko, a traditional Chinese herbal medicine, on fibroblasts and its implication on wound healing processes, Adv. Wound Care 2 (8) (2013) 448–455.

[3] R. Tocmo, J. Pena-Fronteras, K.F. Calumba, M. Mendoza, J.J. Johnson, Valorization of pomelo (Citrus grandis Osbeck) peel: a review of current utilization, phytochemistry, bioactivities, and mechanisms of action, Compr. Rev. Food Sci. Food Saf. 19 (4) (2020) 1969–2012.

[4] Y.-L. Zhao, X.-W. Yang, B.-F. Wu, J.-H. Shang, Y.-P. Liu, D. Zhi, X.-D. Luo, Anti-inflammatory effect of pomelo peel and its bioactive coumarins, J. Agric. Food Chem. 67 (32) (2019) 8810–8818.

[5] A. Zead Helmi, K. Ihab Ibrahim Al, M.M. Shaimaa, A. Asser Ashraf, Phytochemical content and antioxidant activities of pomelo peel extract, Pharmacogn. Res. 11 (3) (2019).

[6] E. Shirakami, S. Yamakawa, K. Hayashida, Strategies to prevent hypertrophic scar formation: a review of therapeutic interventions based on molecular evidence, Burns & Trauma 8 (2020) tkz003.

[7] W. Liu, M. Wang, W. Cheng, W. Niu, M. Chen, M. Luo, C. Xie, T. Leng, L. Zhang, B. Lei, Bioactive antiinflammatory antibacterial hemostatic citrate-based dressing with macrophage polarization regulation for accelerating wound healing and hair follicle neogenesis, Bioact. Mater. 6 (3) (2021) 721–728.

[8] Z. Li, D. Zhu, Q. Hui, J. Bi, B. Yu, Z. Huang, S. Hu, Z. Wang, T. Caranasos, J. Rossi, Injection of ROS-responsive hydrogel loaded with basic fibroblast growth factor into the pericardial cavity for heart repair, Adv. Funct. Mater. 31 (15) (2021), 2004377.

[9] Z. Gan, Z. Xiao, Z. Zhang, Y. Li, C. Liu, X. Chen, Y. Liu, D. Wu, C. Liu, X. Shuai, Y. Cao, Stiffness-tuned and ROS-sensitive hydrogel incorporating complement C5a receptor antagonist modulates antibacterial activity of macrophages for periodontitis treatment, Bioact. Mater. 25 (2023) 347–359.

[10] H. Ding, Y. Cui, J. Yang, Y. Li, H. Zhang, S. Ju, X. Ren, C. Ding, J. Zhao, ROS-responsive microneedles loaded with integrin αvβ6-blocking antibodies for the treatment of pulmonary fibrosis, J. Contr. Release 360 (2023) 365–375.

[11] H. Shan, X. Gao, M. Zhang, M. Huang, X. Fang, H. Chen, B. Tian, C. Wang, C. Zhou, J. Bai, Injectable ROS-scavenging hydrogel with MSCs promoted the regeneration of damaged skeletal muscle, J. Tissue Eng. 12 (2021), 20417314211031378.

[12] C. Wang, J. Wang, X. Zhang, S. Yu, D. Wen, Q. Hu, Y. Ye, H. Bomba, X. Hu, Z. Liu, In situ formed reactive oxygen species–responsive scaffold with gemcitabine and checkpoint inhibitor for combination therapy, Sci. Transl. Med. 10 (429) (2018), eaan3682.

[13] J. Yu, R. Zhang, B. Chen, X. Liu, Q. Jia, X. Wang, Z. Yang, P. Ning, Z. Wang, Y. Yang, Injectable reactive oxygen species-responsive hydrogel dressing with sustained nitric oxide release for bacterial ablation and wound healing, Adv. Funct. Mater. 32 (33) (2022), 2202857.

[14] C. Elliott, The effects of silver dressings on chronic and burns wound healing, Br. J. Nurs. 19 (5) (2010) S32–S36.

[15] D.J. Leaper, Silver dressings: their role in wound management, Int. Wound J. 3 (4) (2006) 282–294.

[16] M. Akter, M.T. Sikder, M.M. Rahman, A.K.M.A. Ullah, K.F.B. Hossain, S. Banik, T. Hosokawa, T. Saito, M. Kurasaki, A systematic review on silver nanoparticles-induced cytotoxicity: physicochemical properties and perspectives, J. Adv. Res. 9 (2018) 1–16.

[17] X. Zhang, Z. Zhang, Q. Shu, C. Xu, Q. Zheng, Z. Guo, C. Wang, Z. Hao, X. Liu, G. Wang, H. Yan, H. Chen, C. Lu, Copper clusters: an effective antibacterial for eradicating multidrug-resistant bacterial infection in vitro and in vivo, Adv. Funct. Mater. 31 (14) (2021), 2008720.

[18] W.-F. Lai, W.-T. Wong, A.L. Rogach, Development of copper nanoclusters for in vitro and in vivo theranostic applications, Adv. Mater. 32 (9) (2020), 1906872.

[19] X. Liu, D. Astruc, Atomically precise copper nanoclusters and their applications, Coord. Chem. Rev. 359 (2018) 112–126.

[20] W. Gong, H.-b. Huang, X.-c. Wang, W.-y. He, Y.-y. Hou, J.-n. Hu, Construction of a sustained-release hydrogel using gallic acid and lysozyme with antimicrobial properties for wound treatment, Biomater. Sci. 10 (23) (2022) 6836–6849.

[21] Y. Kang, C. Xu, X. Dong, M. Qi, D. Jiang, Exosome-functionalized magnesium-organic framework-based scaffolds with osteogenic, angiogenic and anti-inflammatory properties for accelerated bone regeneration, Bioact. Mater. 18 (2022) 26–41.

[22] A.L. Predeina, M.S. Dukhinova, V.V. Vinogradov, Bioreactivity of decellularized animal, plant, and fungal scaffolds: perspectives for medical applications, J. Mater. Chem. B 8 (44) (2020) 10010–10022.

[23] J.K.R. Mutra, S.E. Jujjavarapu, N. Verma, Emergence of plant-based decellularized scaffolds for tissue regeneration: a review, ACS Sustain. Chem. Eng. 11 (17) (2023) 6485–6497.

[24] X. Han, H. Li, D. Zhou, Z. Chen, Z. Gu, Local and targeted delivery of immune checkpoint blockade therapeutics, Accounts Chem. Res. 53 (11) (2020) 2521–2533.

[25] D. Li, J. Li, S. Wang, Q. Wang, W. Teng, Dually crosslinked copper-poly (tannic acid) nanoparticles with microenvironment-responsiveness for infected wound treatment, Adv. Healthcare Mater. (2023), 2203063.

[26] Y. Kim, H. Kim, K. Kim, H.H. Eom, X. Su, J.W. Lee, Electrosorption of cadmium ions in aqueous solutions using a copper-gallate metal-organic framework, Chemosphere 286 (2022), 131853.

[27] B. Azhar, A.E. Angkawijaya, S.P. Santoso, C. Gunarto, A. Ayucitra, A.W. Go, P. L. Tran-Nguyen, S. Ismadji, Y.-H. Ju, Aqueous synthesis of highly adsorptive copper–gallic acid metal–organic framework, Sci. Rep. 10 (1) (2020), 19212.

[28] C. Gunawan, W.Y. Teoh, C.P. Marquis, R. Amal, Cytotoxic origin of copper (II) oxide nanoparticles: comparative studies with micron-sized particles, leachate, and metal salts, ACS Nano 5 (9) (2011) 7214–7225.

[29] H. Tian, J. Yan, W. Zhang, H. Li, S. Jiang, H. Qian, X. Chen, X. Dai, X. Wang, Cu-GA-coordination polymer nanozymes with triple enzymatic activity for wound disinfection and accelerated wound healing, Acta Biomater. 167 (2023) 449–462.

[30] H.U. Zaman, J.M.M. Islam, M.A. Khan, R.A. Khan, Physico-mechanical properties of wound dressing material and its biomedical application, J. Mech. Behav. Biomed. Mater. 4 (7) (2011) 1369–1375.

[31] J.G. Lundin, G.C. Daniels, C.L. McGann, J. Stanbro, C. Watters, M. Stockelman, J. H. Wynne, Multi-functional polyurethane hydrogel foams with tunable mechanical properties for wound dressing applications, Macromol. Mater. Eng. 302 (3) (2017), 1600375.

[32] A. Francesko, D. Soares da Costa, R.L. Reis, I. Pashkuleva, T. Tzanov, Functional biopolymer-based matrices for modulation of chronic wound enzyme activities, Acta Biomater. 9 (2) (2013) 5216–5225.

[33] T. Liu, B. Xiao, F. Xiang, J. Tan, Z. Chen, X. Zhang, C. Wu, Z. Mao, G. Luo, X. Chen, J. Deng, Ultrasmall copper-based nanoparticles for reactive oxygen species scavenging and alleviation of inflammation related diseases, Nat. Commun. 11 (1) (2020) 2788.

[34] D.J. Yang, S.H. Moh, D.H. Son, S. You, A.W. Kinyua, C.M. Ko, M. Song, J. Yeo, Y.-H. Choi, K.W. Kim, Gallic acid promotes wound healing in normal and hyperglucidic conditions, Molecules 21 (7) (2016) 899.

[35] X. Sun, M. Dong, Z. Guo, H. Zhang, J. Wang, P. Jia, T. Bu, Y. Liu, L. Li, L. Wang, Multifunctional chitosan-copper-gallic acid based antibacterial nanocomposite wound dressing, Int. J. Biol. Macromol. 167 (2021) 10–22.

[36] Z. Gan, Z. Xiao, Z. Zhang, Y. Li, C. Liu, X. Chen, Y. Liu, D. Wu, C. Liu, X. Shuai, Stiffness-tuned and ROS-sensitive hydrogel incorporating complement C5a receptor antagonist modulates antibacterial activity of macrophages for periodontitis treatment, Bioact. Mater. 25 (2023) 347–359.

[37] Z.H. Abudayeh, I.I. Al Khalifa, S.M. Mohammed, A.A. Ahmad, Phytochemical content and antioxidant activities of pomelo peel extract, Pharmacogn. Res. 11 (3) (2019).

[38] S. Chen, H. Wang, Y. Su, J.V. John, A. McCarthy, S.L. Wong, J. Xie, Mesenchymal stem cell-laden, personalized 3D scaffolds with controlled structure and fiber alignment promote diabetic wound healing, Acta Biomater. 108 (2020) 153–167.

[39] W. Wan, F. Cai, J. Huang, S. Chen, Q. Liao, A skin-inspired 3D bilayer scaffold enhances granulation tissue formation and anti-infection for diabetic wound healing, J. Mater. Chem. B 7 (18) (2019) 2954–2961.

[40] F. Zhang, Z. Zhang, X. Duan, W. Song, Z. Li, B. Yao, Y. Kong, X. Huang, X. Fu, J. Chang, Integrating zinc/silicon dual ions with 3D-printed GelMA hydrogel promotes in situ hair follicle regeneration, Int. J. Bioprint. 9 (3) (2023).

[41] Y. Zhang, Enhejirigala, B. Yao, Z. Li, W. Song, J. Li, D. Zhu, Y. Wang, X. Duan, X. Yuan, Using bioprinting and spheroid culture to create a skin model with sweat glands and hair follicles, Burns & Trauma 9 (2021) tkab013.

[42] P.D. Mahar, A.B. Spinks, H. Cleland, P. Bekhor, J.S. Waibel, C. Lo, G. Goodman, Improvement of burn scars treated with fractional ablative CO2 lasers—a

systematic review and meta-analysis using the Vancouver Scar Scale, J. Burn Care Res. 42 (2) (2021) 200–206.

[43] C. Liu, R. Lu, M. Jia, X. Xiao, Y. Chen, P. Li, S. Zhang, Biological glue from only lipoic acid for scarless wound healing by anti-inflammation and TGF-β regulation, Chem. Mater. 35 (6) (2023) 2588–2599.

[44] B.C. Carney, J.H. Chen, R.A. Kent, M. Rummani, A. Alkhalil, L.T. Moffatt, D. S. Rosenthal, J.W. Shupp, Reactive oxygen species scavenging potential contributes to hypertrophic scar formation, J. Surg. Res. 244 (2019) 312–323.